Volume 19 | Number 17 | 7 September 2019 | Pages 2761–2948

Lab on a Chip

Devices and applications at the micro- and nanoscale

rsc.li/loc

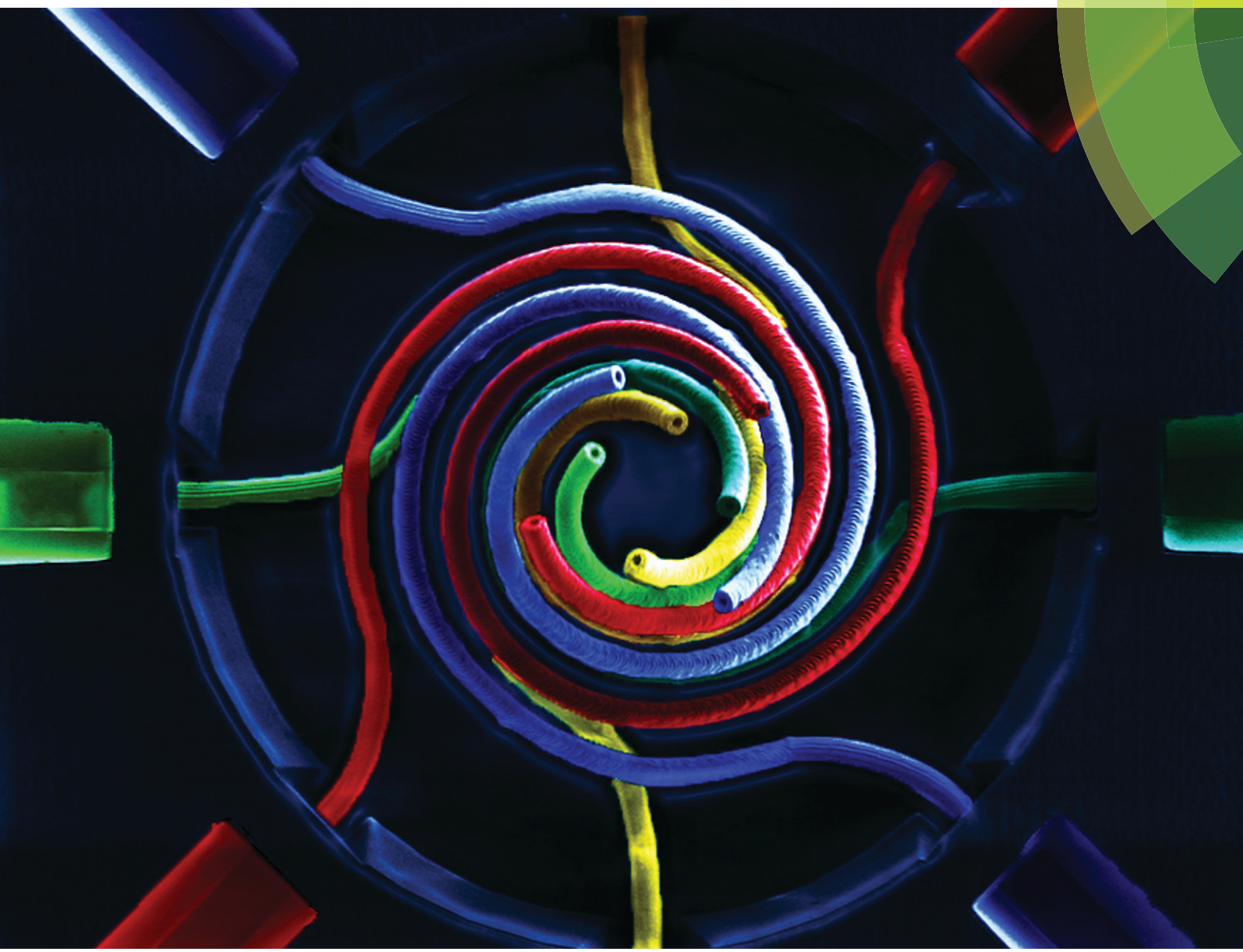

ISSN 1473-0197

ROYAL SOCIETY OF CHEMISTRY | Celebrating IYPT 2019

PAPER
Ryan D. Sochol *et al.*
3D microfluidics *via* cyclic olefin polymer-based *in situ* direct laser writing

Lab on a Chip

PAPER

View Article Online
View Journal | View Issue

Cite this: *Lab Chip*, 2019, **19**, 2799

3D microfluidics *via* cyclic olefin polymer-based *in situ* direct laser writing†

Abdullah T. Alsharhan, [a] Ruben Acevedo,[a] Roseanne Warren[b] and Ryan D. Sochol ‡*[acde]

In situ direct laser writing (*is*DLW) strategies that facilitate the printing of three-dimensional (3D) nanostructured components directly inside of, and fully sealed to, enclosed microchannels are uniquely suited for manufacturing geometrically complex microfluidic technologies. Recent efforts have demonstrated the benefits of using micromolding and bonding protocols for *is*DLW; however, the reliance on polydimethylsiloxane (PDMS) leads to limited fluidic sealing (*e.g.*, operational pressures <50–75 kPa) and poor compatibility with standard organic solvent-based developers. To bypass these issues, here we explore the use of cyclic olefin polymer (COP) as an enabling microchannel material for *is*DLW by investigating three fundamental classes of microfluidic systems corresponding to increasing degrees of sophistication: (i) "2.5D" functionally static fluidic barriers (10–100 μm in height), which supported uncompromised structure-to-channel sealing under applied input pressures of up to 500 kPa; (ii) 3D static interwoven microvessel-inspired structures (inner diameters < 10 μm) that exhibited effective isolation of distinct fluorescently labelled microfluidic flow streams; and (iii) 3D dynamically actuated microfluidic transistors, which comprised bellowed sealing elements (wall thickness = 500 nm) that could be actively deformed *via* an applied gate pressure to fully obstruct source-to-drain fluid flow. In combination, these results suggest that COP-based *is*DLW offers a promising pathway to wide-ranging fluidic applications that demand significant architectural versatility at submicron scales with invariable sealing integrity, such as for biomimetic organ-on-a-chip systems and integrated microfluidic circuits.

Received 7th June 2019,
Accepted 15th July 2019

DOI: 10.1039/c9lc00542k

rsc.li/loc

Introduction

Direct laser writing (DLW) has emerged as an unparalleled 3D manufacturing technology for the fabrication of structures with feature resolutions on the order of 100 nm.[1–3] DLW involves using a tightly focused femtosecond laser and liquid-phase photocurable materials to initiate spatially controlled polymerization events *via* two-photon or multi-photon absorption phenomena (*e.g.*, in a point-by-point, layer-by-layer manner) that ultimately produce 3D microstructures comprised of cured photomaterial.[4,5] A fundamental trade-off inherent to DLW, however, is that the submicron feature size of the curing voxel is poorly suited for fabricating the macro-to-micro interfaces – *i.e.*, inlet and outlet fluidic access ports – that are requisites for DLW-based microfluidic applications.[6,7] To overcome this barrier, researchers have primarily focused on hybrid protocols that rely on standard micromanufacturing methods for bulk device fabrication, with DLW utilized only for critical 3D nanostructured features[8–10] In particular, conventionally manufactured microfluidic channels can be infused with a liquid-phase photocurable material to support DLW-based printing of structures directly inside of the microchannel[11–13] – an approach termed "*in situ* DLW (*is*DLW)".

Previously, researchers have utilized a number of materials for *is*DLW. For example, although glass microchannels are compatible with *is*DLW processes,[14,15] the protocols for manufacturing glass microdevices, such as laser ablation and wet etching (*e.g.*, with HF), are typically associated with undesired fabrication times, costs, labor requirements and/or safety concerns.[16] As a result, many groups have instead focused on the use of PDMS-on-glass microchips for *is*DLW. A drawback of PDMS, however, is that its gas permeability

[a] *Department of Mechanical Engineering, University of Maryland, College Park, MD, 20742, USA*
[b] *Mechanical Engineering, University of Utah, Salt Lake City, UT, 84112, USA*
[c] *Fischell Department of Bioengineering, University of Maryland, College Park, MD, 20742, USA*
[d] *Robert E. Fischell Institute of Biomedical Devices, University of Maryland, College Park, MD, 20742, USA*
[e] *Maryland Robotics Center, University of Maryland, College Park, MD, 20742, USA*

† Electronic supplementary information (ESI) available. See DOI: 10.1039/c9lc00542k

‡ 2147 Glenn L. Martin Hall, University of Maryland, College Park, MD 20742 USA, Email: rsochol@umd.edu.

results in a thin layer of oxygen adjacent to the channel walls, which can inhibit photopolymerization.[17,18]

Although several works have avoided the PDMS interface entirely, instead employing *is*DLW to fabricate structures attached solely to the glass substrate,[19,20] such methods are insufficient for cases that require fluidic sealing along the entire luminal surface of the microchannel. To enable such applications, Lölsberg *et al.* reported that following *is*DLW-based fabrication in a PDMS-on-glass microchip, silane-based epoxy could be perfused through two sacrificial side channels to permeate the gaps between printed structures and the PDMS walls.[21] As an alternative, we recently demonstrated that applying a sol–gel coating to PDMS-on-glass microchannels enabled effective structure-to-channel fluidic sealing for input pressures up to 75 kPa, with the caveat that sealing performance was highly dependent on channel geometry (*e.g.*, size and shape).[22] In addition to limited sealing performance at higher pressures, *is*DLW with PDMS-on-glass microdevices also restricts which developers can be used following the printing process as many conventional DLW developers are organic solvents that can degrade PDMS.[21–23]

To overcome the aforementioned limitations associated with PDMS-on-glass systems while still benefiting from the accessibility of micromolding and bonding procedures, here we examine the use of cyclic olefin polymer (COP) as an alternative microchannel material for *is*DLW. COP is a thermoplastic material that exhibits properties that are advantageous for *is*DLW, including high optical transparency,[24] resistance to polar organic solvents,[25,26] effective micropattern replication and bonding,[27–30] and low gas permeability.[31] We present a novel *is*DLW protocol (Fig. 1) that is based on COP–COP devices fabricated by hot embossing COP using DLW-printed molds with customizable geometries. We experimentally characterize key *is*DLW parameters (*e.g.*, laser power, microchannel shape and size) to elucidate the conditions under which microstructures of various heights can be manufactured effectively. We investigate the performance of COP-based *is*DLW-printed microstructures with hierarchical degrees of geometric and operational microfluidic complexity: (i) monolithic ("2.5D") fluidic barriers that are designed to remain stationary while obstructing fluid flow (irrespective of input pressure) – an important measure of structure-to-channel sealing integrity; (ii) 3D interwoven microvessel-inspired tubular architectures, which while structurally immobile, are designed to permit fluid flow within their internal tortuous microfluidic pathways; and (iii) a 3D

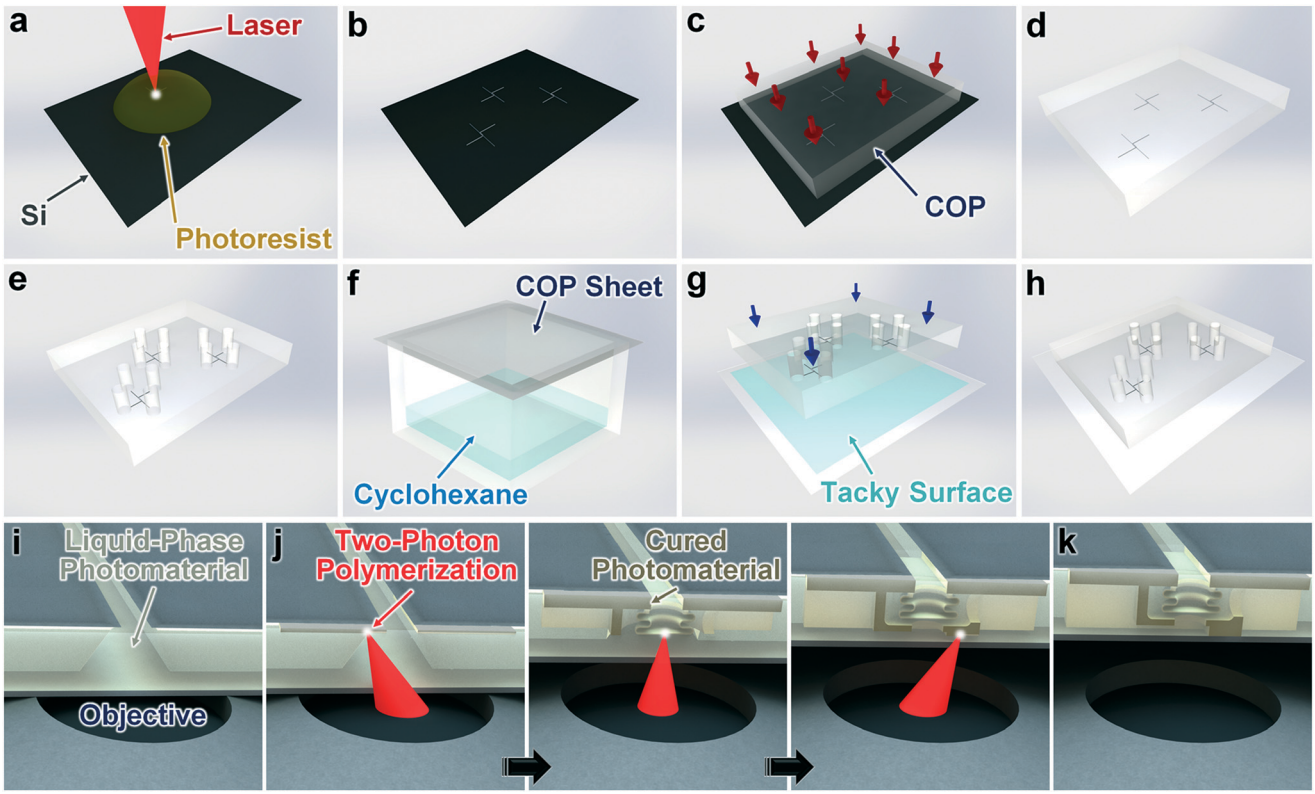

Fig. 1 Conceptual illustrations of the cyclic olefin polymer (COP) *in situ* direct laser writing (*is*DLW) strategy. (a) DLW of microchannel mold structures. (b) Printed negative master mold. (c) Hot embossing-based COP replication of the microchannel molds. (d) Micromolded COP. (e) Integration of inlet and outlet ports. (f) Exposure of vapor-phase cyclohexane to a thin COP sheet. (g) Bonding of the micromolded COP to the thin COP sheet. (h) Enclosed COP–COP microdevice. (i–k) *Is*DLW fabrication. (i) Infusion of a liquid-phase photomaterial into the COP–COP microchannels. (j) "Ceiling-to-floor", point-by-point, layer-by-layer photopolymerization *via* a focused femtosecond IR laser. (k) Printed 3D microfluidic bellow-type transistor (comprised of cured photomaterial) that is fully sealed to the luminal surface of the COP–COP microchannel at designed locations.

microfluidic "bellow-type" transistor that can be dynamically actuated during operation to actively regulate the flow of fluid through the component. The results establish fundamental baselines with which to evaluate the utility of COP-based *is*DLW for a diversity of microfluidic studies and applications.

Materials and methods

Cyclic olefin polymer (COP) *in situ* direct laser writing (*is*DLW) concept

The COP-based *is*DLW approach presented in this work includes five key steps: (i) master mold fabrication *via* DLW (Fig. 1a and b), (ii) mold replication (Fig. 1c and d), (iii) inlet/outlet port integration (Fig. 1e), (iv) COP–COP bonding (Fig. 1f–h), and (v) *is*DLW of microstructures directly inside of (and fully attached to) the COP–COP microchannels (Fig. 1i–k). Several groups have demonstrated the use of DLW for micromold fabrication, particularly for cases that demand non-planar channel geometries.[21,22,32–35] Here, DLW is utilized in the dip-in laser lithography (DiLL) configuration to manufacture microchannels with varying architectures (Fig. 1a). After completion of the mold printing process and development (Fig. 1b), established COP hot embossing methods[36,37] are employed to replicate the microchannel structures (Fig. 1c and d). Thereafter, through holes for inlet and outlet ports are drilled at desired locations in the micromolded COP (Fig. 1e).

A thin, flat COP sheet serves as the base of the COP microchannels. To achieve vapor-phase solvent bonding, the COP base is first exposed to cyclohexane vapor (Fig. 1f), which results in a tacky surface. This surface is then brought into contact with the micromolded COP to achieve fully enclosed COP–COP microchannels (Fig. 1g and h). For the *is*DLW step, a liquid-phase photocurable material is infused into the COP–COP channel (Fig. 1i). DLW is then utilized in the oil-immersion mode for microstructure printing. In this configuration, the laser passes from the objective lens through an immersion oil, then through the thin COP base, and finally, through the uncured photomaterial to begin the photopolymerization process only at the focal point (Fig. 1j). To avoid disruptions of the laser due to interactions with previously cured photomaterial, microstructures are printed in a "ceiling-to-floor", point-by-point, layer-by-layer methodology.[21,22] Once the DLW process is complete (Fig. 1k), developing agents are infused into the channel to remove any remaining uncured photomaterial.

Negative master mold fabrication *via* DLW

All microchannel negative master mold patterns were designed using the commercial computer-aided design (CAD) software, SolidWorks (Dassault Systemes, France). The CAD files were converted to the STL file format, and then imported into the computer-aided manufacturing (CAM) software, DeScribe (Nanoscribe GmbH, Germany) to generate the code for the laser writing path. For all molds, the layer height and hatching parameters were 1 μm and 500 nm, respectively. Si substrates (25 mm × 25 mm) were rinsed successively with acetone and isopropyl alcohol (IPA), then dried with inert N_2 gas, and lastly, placed on a hot plate set at 100 °C for 15 min. The negative-tone photoresist, IP-S (Nanoscribe), was deposited onto the Si substrate, which was then loaded into the Nanoscribe Photonic Professional GT DLW system. The DLW printer settings included the use of a 25× objective lens and the DiLL mode configuration. Due to the large print area of the channel mold structures (approximately 3 mm × 3 mm), a stitching-based print methodology was utilized by which the master mold was printed in 280 μm × 280 μm areas that connect together (*e.g.*, ESI† Fig. S1 and ESI† Movie S1).

For the fluidic barrier structure testing, a total of nine microchannel designs were printed, corresponding to three distinct cross-sectional profiles – each at heights of 10 μm, 50 μm, and 100 μm: (i) rectangular (to mimic channels generated *via* conventional, monolithic microfabrication processes)[38] (ESI† Fig. S2a), (ii) trapezoidal (with 20° outward tapering sidewalls) (ESI† Fig. S2b), and (iii) semi-elliptical (ESI† Fig. S2c). All of the microchannels were designed with an aspect ratio of 1. The molds for the microvessel-inspired structures were designed with a circular region (40 μm in height; 120 μm in diameter) intersecting with six identical microfluidic channels (30 μm in height; 50 μm in width; 25°-tapered trapezoidal cross sections). For the 3D microfluidic transistors, the molds were designed with two intersecting channels (30 μm in height; 50 μm in width; 25°-tapered trapezoidal cross sections). After completion of the DLW-printing process, the substrates were developed using successive rinses in propylene glycol monomethyl ether acetate (PGMEA) for 30 min and IPA for 2 min to remove any remaining uncured photoresist.

COP–COP microdevice fabrication

A 3 mm-thick COP sheet (ZEONOR 1060R, Zeon Corp., Japan) was rinsed with IPA, dried with inert N_2 gas, and then brought into contact with the fabricated negative master mold. The COP sheet was hot embossed for 3 min at 120 °C to facilitate the replication of the microchannel designs from the mold (*e.g.*, ESI† Fig. S2d–f). Through holes for inlet and outlet ports were drilled in the molded COP at desired locations. The surface of a 100 μm-thick COP film (microfluidic ChipShop GmbH, Germany) was exposed to vapor-phase cyclohexane at 30 °C for 2 min. Immediately after the vapor-exposure process, the 100 μm-thick COP film and the micromolded 3 mm-thick COP sheet were brought into contact for 1 min at room temperature (20–25 °C) to facilitate COP–COP bonding, resulting in a final device with enclosed microchannels (ESI† Fig. S3). A key attribute of the 100 μm-thick COP film is that its refractive index (1.53)[39] closely matches that of both borosilicate glass substrates (1.52) and the immersion oil (1.52) that are conventionally used for oil-immersion-mode DLW.

Microstructure fabrication *via is*DLW

The 3D models for the fluidic barrier, microvessel, and microfluidic transistor microstructures were all generated using SolidWorks (Dassault Systemes) and imported into DeScribe (Nanoscribe) for writing-path generation. The negative-tone photoresist, IP-L 780 (Nanoscribe), was vacuum-loaded into the COP–COP microchannels. The microchip was fixed on a holder (with immersion oil placed on the underside of the 100 μm-thick COP film) and loaded into the Nanoscribe Photonic Professional GT DLW system. The DLW printer settings included the use of a 63× objective lens and the oil-immersion mode configuration. All structures were printed *via* a "ceiling-to-floor", point-by-point, layer-by-layer writing-path routine. After completion of the DLW process, any remaining uncured photoresist was cleared from the devices by infusing the organic solvent, PGMEA, for 10 min, IPA for 3 min, and lastly, pressurized air into the microchannels. To facilitate this development process for the circular center region of the microvessel-based COP–COP device, two intervening microchannels (*i.e.*, one input and one output) for developer infusion and material removal were integrated into the design.

Optical characterization

All scanning electron microscopy (SEM) characterizations were carried out using the Hitachi SU-70 Schottky field emission gun SEM (Hitachi, Japan). To facilitate SEM imaging of *is*DLW-fabricated microstructures, the COP–COP bonding and *is*DLW printing protocols were modified to enable detachment of the 100 μm-thick COP base. Specifically, the cyclohexane exposure time was reduced to achieve a relatively weak bond between the 100 μm-thick COP film and the micromolded COP sheet. In addition, printed structures were designed with a slightly smaller height, such that the *is*DLW printing process would terminate approximately 2 μm from the thin COP film (*i.e.*, to prevent the structures from sealing to the base). In combination, these modifications allowed for the 100 μm-thick COP film to be manually removed following the *is*DLW process.

Theoretical simulations

Finite element analysis (FEA) simulations of the 3D microfluidic bellow-type transistor were conducted using the software, COMSOL Multiphysics v.5.3a (COMSOL Inc., Sweden). First, the 3D CAD model was imported into the FEA software, and simulations were performed using the fluid–structure interaction (FSI) module under stokes flow conditions and quasi-static structural transient behavior. The photomaterial, IP-L 780 (E = 1.75 GPa and ν = 0.49),[40] and water ($\rho = 10^3$ kg m^3; $\eta = 8.9 \times 10^{-4}$ Pa s) were modelled for the solid elements and input fluid, respectively. To simulate microfluidic transistor operation, the pressure applied to the gate region was modelled as a boundary load assigned to the internal surface of the bellowed element. The pressure applied to the interior of the bellowed structure was varied from 0 kPa to 90 kPa using a parametric sweep function, while the source fluid input was maintained at a constant pressure of 10 kPa.

Microfluidic experimentation

For all fluidic experiments, MAESFLO software (Fluigent, France) was utilized to interface with the Fluigent Microfluidic Control System (MFCS) and flow rate platform, which supported simultaneous input pressure regulation and pressure/flow rate data registration. Fluids were introduced into the COP microdevices *via* fluorinated ethylene propylene tubing (Cole-Parmer, Vernon Hills, IL) and stainless steel catheter couplers (20 ga., Instech, Plymouth Meeting, PA). For experiments in which specific ports required sealing, stainless steel catheter plugs (Instech) were inserted into the COP through holes. Data from all completed experiments were processed using MATLAB software (MathWorks, Natick, MA) to calculate the mean and standard deviation (S.D.) of the flow rate data with respect to specified input pressure increments corresponding to the fluidic barriers and microfluidic transistor experiments. For testing with fluorescently labelled fluids, methylene blue and rhodamine B dyes (MilliporeSigma, St. Louis, MO) were infused into the microdevices *via* distinct inlet ports. Microscopic imaging was performed using an inverted microscope (Motic AE31, Motic, Canada) connected to a charge-coupled device (CCD) camera (Moticam Pro 285B, Motic), while fluorescence imaging was performed using an inverted fluorescence microscope (Axio Observer.Z1, Zeiss, Germany) connected to a CCD camera (Axiocam 503 Mono, Zeiss).

Results and discussion

COP-based *is*DLW fabrication parameters

An important criteria for *is*DLW is that the base material through which the laser passes must have sufficient optical transparency such that photopolymerization phenomena are not disrupted significantly, particularly for microstructures printed at taller heights (*i.e.*, farther away from the objective lens). Although the "ceiling-to-floor" printing strategy employed in this work limits laser aberrations caused by previously cured microstructures in the laser path, remaining factors – namely, the optical properties of the uncured photoresist and the thin COP base – could still disrupt DLW-based photopolymerization events. Experiments in which the laser power was held constant during the *is*DLW fabrication process revealed malformed microstructures for which components at taller heights did not appear to cure effectively (*e.g.*, ESI† Fig. S4). To overcome such issues, two key parameters can be dynamically adjusted: (i) increasing the laser power with increasing height, or (ii) decreasing the laser scanning speed with increasing height. To maintain a consistent overall print time, it is preferable to first set the scanning speed at a constant magnitude (10 mm s^{-1} in this case), and then vary the laser power accordingly. A challenge in determining the appropriate laser power for a given height is that the exposure energy must be large enough to effectively initiate

photopolymerization reactions, yet not too large such that photomaterial burning failures (*e.g.*, disruptive microbubble generation) occur.

We conducted fabrication experiments at varying heights and laser powers, and then performed optical characterizations of the results to establish an optimal parameter space for COP-based *is*DLW. The fabrication data suggest an exponential relationship between the laser power and the *is*DLW height in the form of:

$$P = 16.9e^{(9.1\times10^{-3})H} \quad (1)$$

where P is the laser power in mW and H is the writing height in μm measured as the distance from the COP base surface of the microchannel (Fig. 2a). It is important to note that these results are based on a specific set of materials (*e.g.*, 100 μm-thick COP substrate, IP-L 780 photoresist) and DLW printing parameters (*e.g.*, 300 nm layer height, 200 nm hatching distance, 10 mm s^{-1} scanning speed), and that any changes to such conditions may alter the observed laser power-height correlation. Nonetheless, by using this data to vary the laser power with printing height (using 10 μm intervals), we observed that microstructures could be successfully fabricated in COP–COP channels with heights ranging from 10 μm up to 100 μm (*e.g.*, ESI† Fig. S5 and ESI† Movie S2).

Both the height and the shape of the microchannel cross-sectional profile – in particular, the degree of sidewall tapering – can significantly affect the efficacy of *is*DLW with respect to structure-to-channel sealing integrity. While we,[22] and other groups,[21] have previously hypothesized that the sidewalls of microchannel profiles that lack significant outward tapering induce a "shadowing" effect that disrupts the laser path (*i.e.*, preventing *is*DLW in proximity to the sidewalls), the inability to remove the channel base following *is*DLW prevented confirmation of such phenomena.[21,22] To investigate the potential for shadowing events to contribute to *is*DLW structure-to-channel sealing failures, here we utilized a weak COP–COP bonding approach to enable facile removal of the 100 μm-thick COP film following the *is*DLW printing process, thereby allowing for optical characterization of the *in situ* fabrication results.

For negative master mold fabrication, conventional photolithography-based methods are considerably faster than the point-by-point, layer-by-layer DLW approach utilized in this work. The caveat to the use of such microfabrication processes, however, is that the resulting microchannels typically exhibit relatively straight sidewalls.[38] To explore the applicability of monolithic microfabrication protocols for *is*DLW, we fabricated COP–COP microdevices with rectangular channel cross sections at varying heights, and then printed 10 μm-thick microstructures designed to fully adhere along the top and sidewall surfaces of the microchannel (Fig. 2b). The fabrication results revealed that for 100 μm-tall channels, a significant portion of the microstructure did not appear to effectively photopolymerize in the regions adjacent to the sidewalls (Fig. 2b – left), despite the laser scanning in these locations (ESI† Fig. S5a and ESI† Movie S2a). Although not as drastic, similar photocuring failures in proximity to the sidewalls at taller heights also occurred for cases with 50 μm-tall channels (Fig. 2b – middle). In contrast, for the 10 μm-tall rectangular microchannels, we did not observe any such fabrication issues (Fig. 2b – right). These results suggest that conventional microfabrication protocols for negative master mold manufacturing should only be utilized in cases of *is*DLW corresponding to microchannels with small heights (*e.g.*, 10 μm). One note, however, is that the replicated COP can also be used to micromold PDMS, which can then serve as an alternative negative master mold to extend the overall lifespan of the DLW-fabricated mold (see also ESI† Text and ESI† Fig. S6).

In addition to the rectangular channel profiles, we also investigated COP–COP microchannels of varying heights with trapezoidal (20°-tapered) and semi-elliptical cross sections (Fig. 2c and d). Unlike the rectangular channel results, we did not observe any height-based disparities in microstructure polymerization adjacent to the sidewalls. Rather, for both the trapezoidal and semi-elliptical cases, the *is*DLW

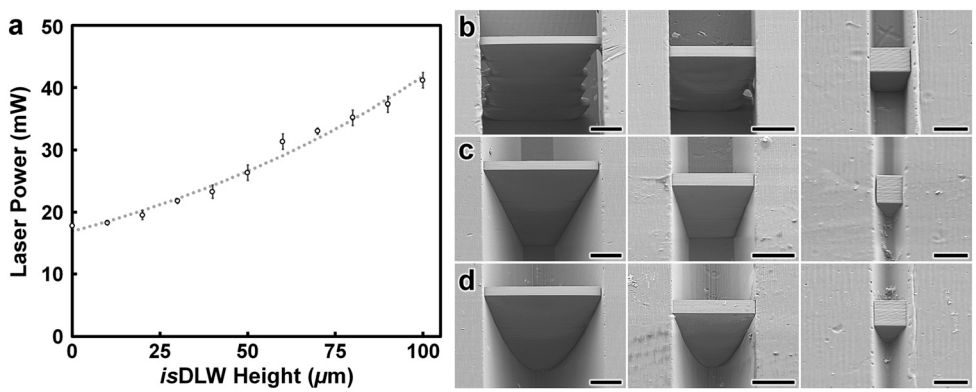

Fig. 2 *Is*DLW fabrication results for fluidic barrier microstructures. (a) Average laser power associated with successful *is*DLW prints and distinct heights (while maintaining a constant laser scanning speed). Dotted line represents eqn (1); error bars = S.D. for n = 3 experiments. (b–d) SEM micrographs of fluidic barrier structures printed in COP–COP channels with (b) rectangular, (c) trapezoidal, and (d) semi-elliptical profiles corresponding to channel heights of: (left) 100 μm, (middle) 50 μm, and (right) 10 μm. Scale bars = (left, middle) 25 μm; (right) 10 μm.

results revealed undisrupted microstructure prints along the entire top and sidewall surfaces of the microchannels for every height examined (Fig. 2c and d). In combination, these fabrication results suggest that for tall microchannels (*e.g.*, ≥50 μm), conventional microfabrication protocols for master mold construction are ill suited for *is*DLW processes in which microstructures are printed in proximity to the channel sidewalls. For such cases, alternative methods of negative master mold fabrication that yield microchannels with effectively tapered sidewalls (*e.g.*, *via* DLW) should be utilized instead.

2.5D static microstructure case: microfluidic barriers

A critical metric of performance for *is*DLW strategies is the fluidic sealing integrity, which is related to the degree of structure-to-channel adhesion along the entire luminal surface of the microchannel. To quantify the sealing behavior for COP-based *is*DLW, we performed microfluidic burst-pressure experiments in which a ramping input pressure was applied on one side of an *is*DLW-printed barrier structure (with a plug in the other port on the same side), while both outlets on the opposite side of the barrier remained open (Fig. 3a and b). While gradually increasing the input pressure at a rate of 2 kPa s^{-1}, we optically monitored the 10 μm-thick barrier to evaluate if the dye-colored fluid remained on one side of the structure (*e.g.*, Fig. 3c) or if fluid leaked past the structure at a particular pressure magnitude. In addition, we also recorded both the input pressure and fluid flow rates during experimentation to measure any degree of fluid leakage.

Experiments with barrier microstructures printed inside COP–COP microchannels with rectangular cross sections revealed a significant role of channel height in the fluidic sealing performance (Fig. 3d). Unlike typical burst-pressure tests in which fluid flow is blocked up until a critical pressure at which point the flow rate instantaneously increases dramatically, the data from experiments with the two larger rectangular microchannels did not exhibit such fluidic events. Specifically, from the onset of experimentation for the 50 μm and 100 μm cases, we observed a linear relationship between the applied input pressure and the rate of fluid flow leaking past the barrier structure (Fig. 3d). This flow behavior suggests that the barriers lacked structure-to-channel sealing prior to experimentation, which is consistent with the results of the malformed barrier microstructures immediately after *is*DLW fabrication (Fig. 2b – left and middle). For the 10 μm case, however, we did not observe fluidic leakage past the barrier for input pressures up to approximately 500 kPa – the limit of the pressure regulator equipment, and thus, the largest pressures examined (Fig. 3d). This sealing efficacy is also corroborated by the fabrication results (Fig. 2b – right).

To investigate the structure-to-channel sealing integrity associated with COP–COP microchannels with non-planar sidewalls, we *is*DLW-printed fluidic barrier microstructures in channels with trapezoidal (20°) and semi-elliptical (aspect ratio = 1) cross-sectional profiles of varying heights. In contrast to the rectangular cases, the burst-pressure experiments with trapezoidal and semi-elliptical COP–COP channels did not reveal any such differences in sealing performance as a function of

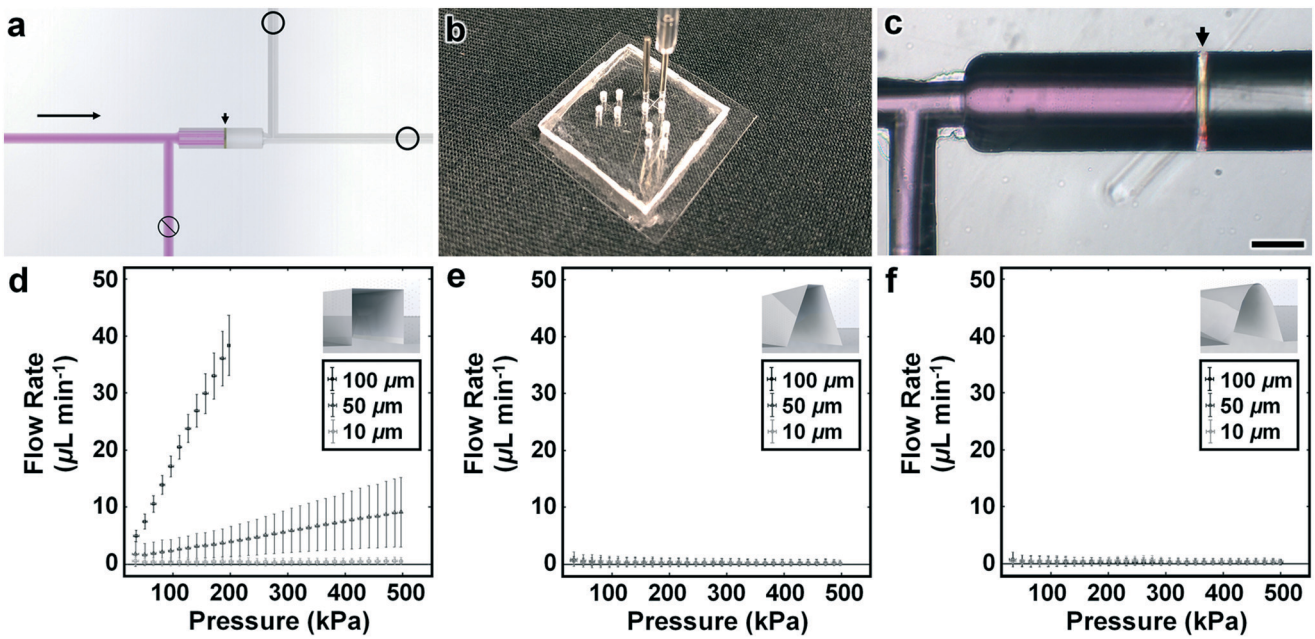

Fig. 3 Microfluidic burst-pressure experimental results for *is*DLW-printed barrier structures. (a) Conceptual illustration of the experimental setup. Long arrow denotes the direction of input pressure; short arrow marks the location of the fluidic barrier structure in the channel. (b) Image of a device prepared for experimentation. (c) Micrograph of fluidic sealing under an applied input pressure of 500 kPa. Short arrow marks the location of the fluidic barrier structure in a 100 μm-tall trapezoidal channel. Scale bar = 50 μm. (d–f) Quantified experimental results corresponding to channels with varying heights and (d) rectangular, (e) trapezoidal, and (f) semi-elliptical profiles. Error bars = S.D. for n = 9 experiments per channel height and profile.

microchannel height (Fig. 3d–f). Notably, for the pressure ranges investigated (*i.e.*, ≤500 kPa), we did not observe any instances of fluidic barrier rupture for the 10 μm, 50 μm, and 100 μm cases corresponding to both the trapezoidal and semi-elliptical microchannel profiles (Fig. 3e and f). With respect to comparable PDMS-based *is*DLW results from prior work,[22] the burst-pressure results – particularly for the 50 μm and 100 μm channels – represent an order of magnitude improvement in fluidic sealing performance.

Although a number of factors may have contributed to the significant enhancement in fluidic sealing integrity associated with *is*DLW in COP–COP microchannels *versus* PDMS-based systems, one key difference is the mechanical stiffness of COP compared to PDMS. Due to the relatively low elasticity of PDMS, inputting pressures on the order of 10–100 kPa results in visible outward expansion of microfluidic channels. As the microchannels expand, *is*DLW-printed barrier microstructures would be subjected to additional axial loading along the PDMS channel-to-structure interface. Microchannels comprised of COP – which has a Young's modulus that is approximately three orders of magnitude larger than that of PDMS – do not exhibit such deformations, including at pressure ranges up to 500 kPa. The lack of channel expansion-based axial forces for COP–COP systems restricts the overall mechanical loading on an *is*DLW-printed fluidic barrier structure to forces deriving solely from the pressure drop across the barrier.

3D static microstructure case: interwoven microvessel-inspired microfluidics

Although the microfluidic barrier structures provide a model system with which to interrogate structure-to-channel sealing behavior, we anticipate that COP-based *is*DLW is better suited for microfluidic applications that rely on architectures with greater extents of geometric complexity. To explore the potential use of COP-based *is*DLW for such scenarios, we designed

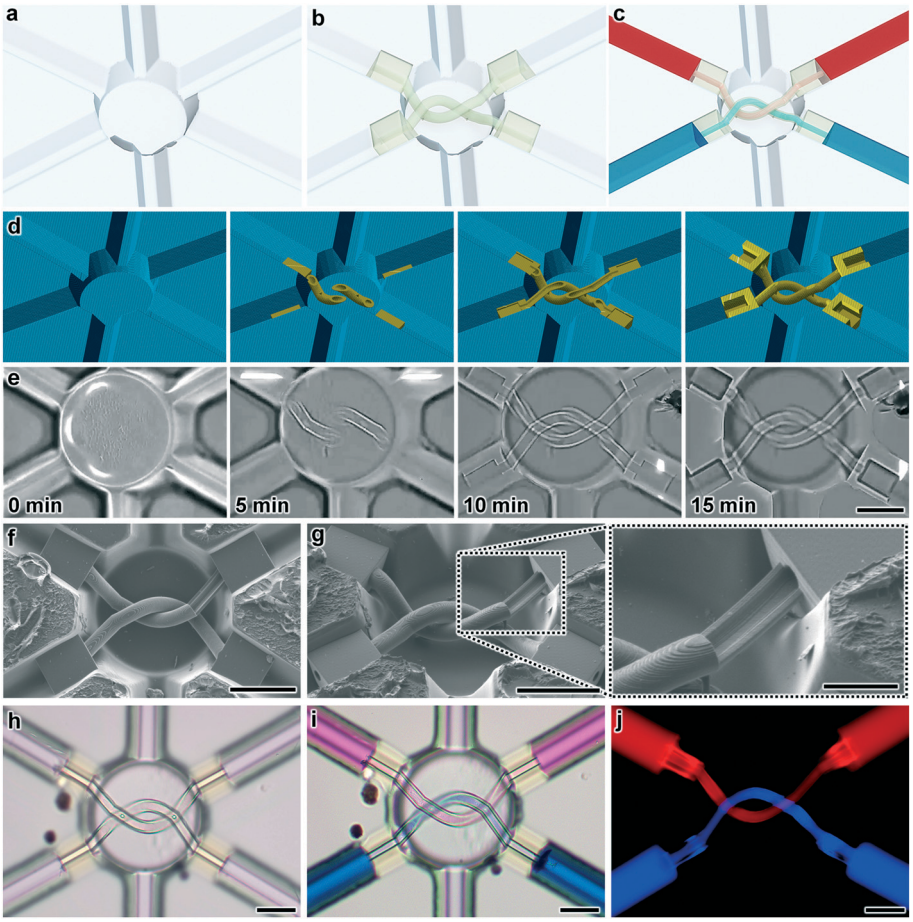

Fig. 4 Results for COP-based *is*DLW-printed interweaving 3D microvessel-inspired microstructures. (a–c) Conceptual illustrations of the: (a) empty COP–COP microchannel, (b) *is*DLW-printed microvessel structures, and (c) independent loading of distinct fluorescently labelled fluids. (d and e) Sequential images of (d) CAM simulations, and (e) corresponding fabrication results for the *is*DLW printing process (see also ESI† Movie S3). Scale bar = 50 μm. (f and g) SEM micrographs of fabrication results for *is*DLW-printed microvessel structures designed with one unenclosed tubular region. (f) Top view. (g) Tilted orientation with expanded view of the unenclosed region. Scale bars = 50 μm; (expanded view) 20 μm. (h–j) Experimental results of the microvessel structures: (h) prior to microfluidic loading, and (i) after microfluidic loading of rhodamine B-labelled fluid (pink) and methylene blue-labelled fluid (blue) (see also ESI† Movie S4). Scale bars = 50 μm. (j) Fluorescence micrographs of the microvessel structures filled with distinctly labelled fluids (see also ESI† Fig. S7). Red = rhodamine B; blue = methylene blue; scale bar = 50 μm.

a microfluidic system comprising two interwoven microvessel-inspired components – each with an inner diameter of 8 μm and a wall thickness of 2 μm – and examined the manufacturability of the tubular, tortuous 3D microstructures within COP microchannels (Fig. 4a and b) as well as their ability to isolate distinct fluorescently labelled microfluidic flow streams (Fig. 4c).

CAM simulations and corresponding printing results for the "ceiling-to-floor", point-by-point, layer-by-layer microvessel *is*DLW fabrication process (within COP–COP microchannels) are presented in Fig. 4d and e, respectively (see also ESI† Movie S3). To prevent disruptions to the laser path caused by previously photocured structures, both microvessel-inspired structures were manufactured simultaneously. SEM micrographs of the fabrication results revealed effective production of the intricate 3D architectures, including the 8 μm-diameter microcurvature of the luminal surface of the vessel structure and the 2 μm-thick microvessel walls (Fig. 4f and g).

To evaluate the microfluidic integrity of the fully enclosed microvessel-inspired structures, we configured the device such that: (i) one microchannel with a microvessel interface was connected to an input with a rhodamine B-dyed fluid, (ii) one microchannel interfacing with the other microvessel structure was connected to a methylene blue-dyed fluid input, and (iii) the four additional access ports – including those corresponding to the two intervening microchannels not directly connected to any microvessel structures (whose function is to support uncured photoresist removal) – remained open (Fig. 4h). We then perfused both the rhodamine B-dyed fluid and the methylene blue-dyed fluid independently through their respective microvessel structures (Fig. 4i; ESI† Movie S4). Fluorescence micrographs of the microfluidic system confirmed that the flow streams were uncompromised (*i.e.*, leakage/contamination between the discrete microvessels or the intervening microchannels did not occur), with distinct fluorescence signatures corresponding to each microvessel structure (Fig. 4j; ESI† Fig. S7). As recent efforts based on alternative additive manufacturing approaches have faced difficulties in recreating fully 3D interweaving tubular structures at sub-100 μm scales,[41–43] these results suggest that the presented COP-based *is*DLW strategy could serve as an enabling technology for organ-on-a-chip systems that require physiologically accurate 3D nanostructured microfluidic components. One caveat to the fluorescence experimentation is that the photomaterial in this study exhibits autofluorescence at lower wavelengths (*e.g.*, 405 nm and 480 nm); however, as researchers have demonstrated DLW-based manufacturing with a wide range of photomaterials – including those that lack autofluorescence at such wavelengths – applications that rely on detecting fluorescence properties should utilize alternative photomaterials for *is*DLW.[44,45]

3D dynamic microstructure case: microfluidic bellow-type transistors

The manufacturing of 3D microfluidic systems that comprise active valving elements represents an exemplar with which to investigate the efficacy of COP-based *is*DLW in situations that simultaneously demand sophisticated architectures as well as functionalities.

Here we designed and printed a 3D microfluidic bellow-type transistor inside of COP–COP microchannels that consists of two fundamental regions: (i) a source-to-drain flow path that includes a centrally located top orifice for source fluid entry and a laterally positioned orifice for the drain output, and (ii) a separate gate area that includes a 3D bellowed microstructure (Fig. 5a). Under an applied source pressure (P_S), the fluid flow through the microfluidic transistor is unobstructed, passing through the top orifice, bypassing the bellowed component, and then flowing out of the lateral orifice (Fig. 5a – left). In contrast, when a gate pressure (P_G) of sufficient magnitude is applied, the 3D bellowed component deforms such that its top surface interacts with the source orifice to physically obstruct source-to-drain fluid flow (Q_{SD}) (Fig. 5a – right).

We performed FEA FSI simulations with a constant P_S of 10 kPa while gradually increasing P_G to provide insight into the mechano-fluidic interactions that govern the operational performance of the microfluidic bellow-type transistor (Fig. 5b; ESI† Movie S5). Initially for P_G = 0 kPa, Q_{SD} was at its maximum value (Fig. 5b – left). As P_G increased, however, the bellowed structure deformed toward the source orifice, thereby increasing the hydraulic resistance through the microfluidic transistor and reducing the magnitude of Q_{SD} (ESI† Movie S5). For $P_G > 90$ kPa, we observed complete obstruction of Q_{SD} based on contributions from two components of the bellowed microstructure: (i) deformations stemming from the bellows, and (ii) expansion of its top surface into the orifice (Fig. 5b – right). Although the simulation results for an ideal microfluidic transistor revealed full sealing due to interactions along a single circular edge, it is likely that full Q_{SD} obstruction during experimentation would require a higher degree of contact between the top surface of the bellowed microstructure and the surfaces adjacent to the source orifice.

To experimentally characterize the 3D microfluidic bellow-type transistor, we printed the component at a t-junction of a COP–COP device with trapezoidal microchannels of 30 μm in height (Fig. 5c and d; ESI† Movie S6). SEM micrographs of a printed cross section revealed effective fabrication of the 500 nm-thick walls of the bellowed microstructure and the 2 μm gap between the bottom surface of the source orifice and the top surface of the bellowed structure, with an absence of stiction-based failure modes (*e.g.*, premature sealing to the source orifice, collapsing of the bellowed components) (Fig. 5e). During experimental actuation of the *is*DLW-printed microfluidic transistor, varying the magnitude of P_G resulted in optically observable deformations of the bellowed microstructure (Fig. 5f; ESI† Movie S7).

We quantified the operational performance of the microfluidic transistor by varying P_S at increasing increments of P_G while monitoring the corresponding Q_{SD} (Fig. 5g). For P_G ranging from 0 kPa to 100 kPa, increasing P_G resulted in

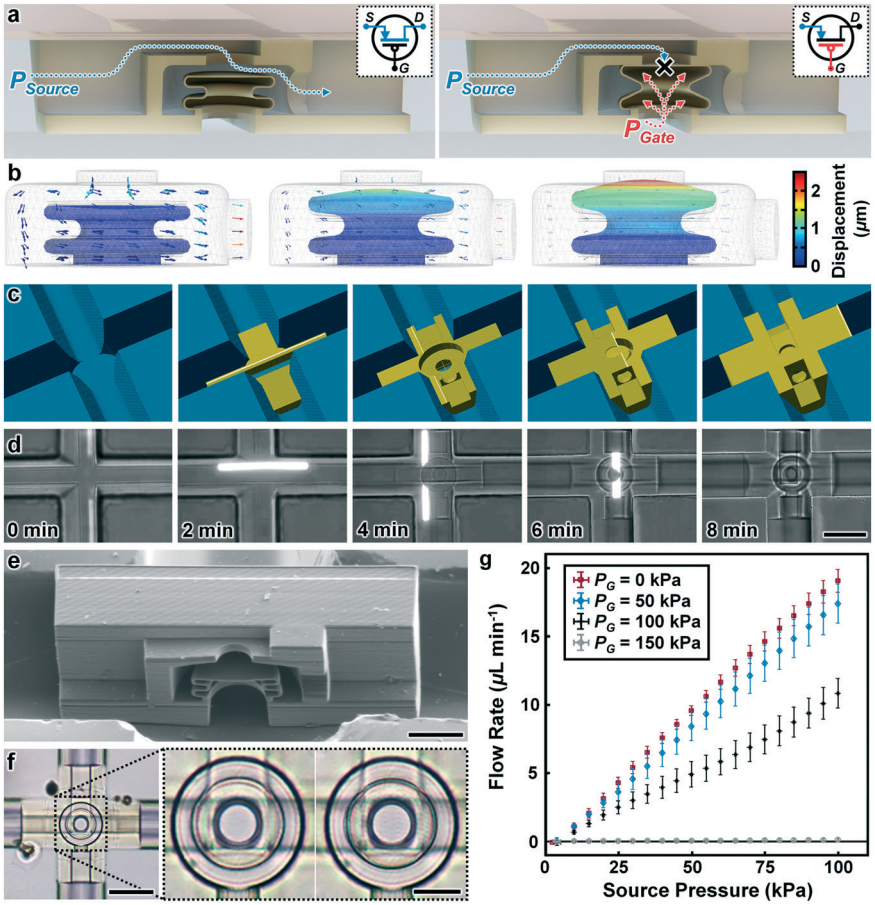

Fig. 5 Results for the COP-based *is*DLW-printed 3D microfluidic bellow-type transistor. (a) Conceptual illustrations of the operating principle. (Left) In the absence of a gate pressure (P_G), the source pressure (P_S) drives fluid flow through the microfluidic transistor. (Right) An applied P_G causes the bellowed microstructure to expand and physically block fluid flow through the microfluidic transistor. Insets include analogous electronic circuit symbols. (b) Sequential 3D COMSOL Multiphysics fluid–structure interaction (FSI) simulation results for fluid velocity field (colored arrows) and displacement distribution for the microfluidic transistor with P_S = 10 kPa and P_G increasing from (left) 0 kPa to (right) 90 kPa (see also ESI† Movie S5). (c and d) Sequential images of (c) CAM simulations, and (d) corresponding fabrication results for the *is*DLW printing process (see also ESI† Movie S6). Scale bar = 50 μm. (e) SEM micrograph of fabrication results for an *is*DLW-printed microfluidic transistor cross section. Scale bar = 15 μm. (f) Micrographs of the microfluidic transistor during operation. Expanded views: (left) P_G = off; (right) P_G = on. Scale bars = 50 μm; (expanded view) 15 μm. (see also ESI† Movie S7). (g) Experimental results for source-to-drain fluid flow (Q_{SD}) *versus* P_S for varying P_G. Error bars = S.D. for n = 3 experiments.

slight reductions in the relatively linear relationships between Q_{SD} and P_S (Fig. 5g). This behavior is an indication of increasing hydraulic resistance through the source-to-drain flow path within the microfluidic transistor, which is consistent with the simulation results (Fig. 5b; ESI† Movie S5). For P_G = 150 kPa, however, the experimental results revealed a full discontinuation of Q_{SD} (Fig. 5g).

One potential basis for the observed trends for $P_G \leq 100$ kPa cases in which $P_G \gg P_S$ (*e.g.*, P_G = 100 kPa; P_S = 25 kPa), yet Q_{SD} persisted (Fig. 5g) is the effective mechanical stiffness of the bellowed microstructure. Specifically, sealing of the source orifice requires a sufficient magnitude of P_G to fully deform the bellowed structure such that the top surface displaces the complete distance from its initial state to the orifice (Fig. 5a). In this study, we observed that P_G = 150 kPa facilitated the desired functionality (Fig. 5g); however, it is important to note that the active sealing functionality of the 3D microfluidic bellow-type transistor can be readily tuned *via* geometric modifications. For example, the effective stiffness of the bellowed element can be reduced by increasing the number of bellows, thereby resulting in comparatively larger displacements for a given P_S. Alternatively, the designed distance from the top surface of the bellowed structure to the source orifice can be decreased to limit the amount of deformation required for the initiation of bellow-orifice interactions.

Conclusions

Submicron-scale additive manufacturing or "3D printing" approaches hold significant promise for the microfluidics community; however, without facile methods that allow for fluidic access to printed components (*i.e.*, *via* macro-to-micro interfaces), the utility of such technologies remains limited.

Although recent efforts have demonstrated PDMS-based *is*DLW strategies as potential solutions, drawbacks inherent to PDMS as a material (*e.g.*, gas permeability, poor compatibility with organic solvents, elasticity) render it poorly suited for *is*DLW of microfluidic systems (*e.g.*, Fig. S8a–c; ESI† Movie S8). In this work, we investigated the use of COP as an enabling material for *is*DLW due to a number of shared benefits with PDMS (*e.g.*, capacity for micromolding and bonding, optical transparency), while overcoming several of the key limitations. The low gas permeability of COP allowed for microstructures to be *is*DLW-printed directly onto native COP surfaces (*e.g.*, Fig. S8d–i; ESI† Movie S9), bypassing the need for extraneous microchannel processing steps, such as pre-process application of surface coatings[22] or post-process loading of silane-based glues through sacrificial channels.[21] The high resistance of COP to organic solvents facilitated the use of standard DLW developers (*e.g.*, PGMEA), thereby avoiding the need for undesired alterations to development protocols based solely on microchannel material incompatibility.[21–23] In addition, the relatively high Young's modulus of COP (>1 GPa) prevented pressure-based microchannel deformations that can exert undesired axial loading on microstructure-to-channel interfaces and lead to premature fluidic sealing failures.

In this work, we systematically explored the use of COP-based *is*DLW for 3D microfluidic scenarios corresponding to hierarchical degrees of structural and functional system complexity. As a fundamental baseline, we printed monolithic 10 μm-thick fluidic barrier structures inside of COP–COP microchannels of varying cross-sectional profiles. For the trapezoidal and semi-elliptical channels in particular, burst-pressure experiments revealed consistent microfluidic sealing for input pressures up to 500 kPa independent of microchannel height (Fig. 3e and f) – an order of magnitude improvement compared to the state of the art.[22] Notably, the 500 kPa limit was a constraint of the experimental setup, and thus, it is possible that COP-based *is*DLW-printed microstructures are able to withstand significantly higher pressures.

We also fabricated interweaving microvessel-inspired architectures with inner diameters <10 μm to assess COP-based *is*DLW of 3D microfluidic systems in which the overall structure remains static during operation. To our knowledge, no prior report has demonstrated geometrically complex, biomimetic microfluidic structures at such scales with full micro-to-macro integration. This ability to recreate anatomical microfluidic systems at physiologically accurate length scales could provide a promising pathway not only to the manufacturing of biological phantoms (*e.g.*, with microvasculature),[46–48] but also toward cellularized *in vitro* platforms, such as for modeling components of the kidney, liver, and/or blood–brain barrier.[41,42,49] In addition, the presented strategy can be employed with a wide range of DLW-compatible photomaterials, including those that are flexible and optically transparent.[50–52] Such features are beneficial for biological applications, particularly for cases in which cell imaging is desired.[53]

To provide insight into the use of COP-based *is*DLW for printing 3D microfluidic systems capable of dynamic operations *via* active control schemes, we designed and characterized a novel microfluidic bellow-type transistor within 30 μm-tall COP–COP channels. For a sufficiently large P_G, the experimental results revealed full blocking of fluid flow through the microfluidic circuit element (Fig. 5g). As the operational performance of the microfluidic transistor is a function of the geometric design of the bellowed component, the concepts established here could be extended to enable 3D integrated microfluidic circuits comprising microfluidic transistors with differing bellow structures designed to activate at distinct P_G magnitudes – an approach that could overcome the "tyranny of microfluidic interconnects" at unprecedented length scales.[54,55] At present, however, the reported microfluidic bellow-type transistor represents, to the best of our knowledge, the smallest 3D printed active microfluidic valving component reported in the literature.[55–58]

By circumventing conventional clean room-based microfabrication protocols (as the micromolding and *is*DLW steps rely primarily on DLW-based fabrication), the COP-based *is*DLW strategies described in this work can be employed by any researcher with access to a DLW printer. Consistent with the benefits of 3D printing, researchers can readily disseminate electronic files of 3D models to enable rapid on-site printing of new microfluidic systems.[55–59] In combination, COP-based *is*DLW offers unique capabilities and accessibility for investigators to harness the vast submicron-scale geometric versatility of DLW for emerging microfluidic studies and applications.

Author contributions

All authors conceived the methodologies in the manuscript. A. A. led the efforts to design, fabricate, simulate, test, and analyze data for the microfluidic barriers, microvessels, and microfluidic transistor. R. A. led the effort to produce CAD models and conceptual illustrations for the microvessels and microfluidic transistor and contributed in the effort to test the microfluidic barriers. All authors prepared and reviewed the manuscript.

Conflicts of interest

The authors declare no conflicts of interest.

Acknowledgements

We greatly appreciate the contributions of Andrew Lamont, Michael Restaino, Siddhartha Das, and the members of the Bioinspired Advanced Manufacturing (BAM) Laboratory. We also greatly appreciate the help and support of technical staff and members of the Maryland Nanocenter and Terrapin Works. This work is supported in part by NSF Award Numbers 1761395 and 1761273.

References

1 A. E. Goodling, S. Nagelberg, B. Kaehr, C. H. Meredith, S. I. Cheon, A. P. Saunders, M. Kolle and L. D. Zarzar, *Nature*, 2019, **566**, 523.
2 M. Hippler, E. Blasco, J. Qu, M. Tanaka, C. Barner-Kowollik, M. Wegener and M. Bastmeyer, *Nat. Commun.*, 2019, **10**, 232.
3 D. Nishiguchi, I. S. Aranson, A. Snezhko and A. Sokolov, *Nat. Commun.*, 2018, **9**, 4486.
4 P.-I. Dietrich, M. Blaicher, I. Reuter, M. Billah, T. Hoose, A. Hofmann, C. Caer, R. Dangel, B. Offrein, U. Troppenz, M. Moehrle, W. Freude and C. Koos, *Nat. Photonics*, 2018, **12**, 241–247.
5 T. Gissibl, S. Thiele, A. Herkommer and H. Giessen, *Nat. Photonics*, 2016, **10**, 554–560.
6 E. Montinaro, M. Grisi, M. Letizia, L. Pethö, M. Gijs, R. Guidetti, J. Michler, J. Brugger and G. Boero, *PLoS One*, 2018, **13**, e0192780.
7 R. D. Sochol, E. Sweet, C. C. Glick, S.-Y. Wu, C. Yang, M. Restaino and L. Lin, *Microelectron. Eng.*, 2018, **189**, 52–68.
8 Y. He, B.-L. Huang, D.-X. Lu, J. Zhao, B.-B. Xu, R. Zhang, X.-F. Lin, Q.-D. Chen, J. Wang and Y.-L. Zhang, *et al.*, *Lab Chip*, 2012, **12**, 3866–3869.
9 T. W. Lim, Y. Son, Y. J. Jeong, D.-Y. Yang, H.-J. Kong, K.-S. Lee and D.-P. Kim, *Lab Chip*, 2011, **11**, 100–103.
10 J. Wang, Y. He, H. Xia, L.-G. Niu, R. Zhang, Q.-D. Chen, Y.-L. Zhang, Y.-F. Li, S.-J. Zeng and J.-H. Qin, *et al.*, *Lab Chip*, 2010, **10**, 1993–1996.
11 M. H. Olsen, G. M. HjortÃÿ, M. Hansen, Z. Met, I. M. Svane and N. B. Larsen, *Lab Chip*, 2013, **13**, 4800.
12 D. Wu, L.-G. Niu, S.-Z. Wu, J. Xu, K. Midorikawa and K. Sugioka, *Lab Chip*, 2015, **15**, 1515–1523.
13 D. Wu, J. Xu, L.-G. Niu, S.-Z. Wu, K. Midorikawa and K. Sugioka, *Light: Sci. Appl.*, 2015, **4**, e228.
14 K. Sugioka, J. Xu, D. Wu, Y. Hanada, Z. Wang, Y. Cheng and K. Midorikawa, *Lab Chip*, 2014, **14**, 3447–3458.
15 D. Wu, S.-Z. Wu, J. Xu, L.-G. Niu, K. Midorikawa and K. Sugioka, *Laser Photonics Rev.*, 2014, **8**, 458–467.
16 H. Wang, Y.-L. Zhang, W. Wang, H. Ding and H.-B. Sun, *Laser Photonics Rev.*, 2017, **11**, 1600116.
17 S. E. Chung, W. Park, S. Shin, S. A. Lee and S. Kwon, *Nat. Mater.*, 2008, **7**, 581–587.
18 J. R. Tumbleston, D. Shirvanyants, N. Ermoshkin, R. Janusziewicz, A. R. Johnson, D. Kelly, K. Chen, R. Pinschmidt, J. P. Rolland and A. Ermoshkin, *et al.*, *Science*, 2015, aaa2397.
19 M. Iosin, T. Scheul, C. Nizak, O. Stephan, S. Astilean and P. Baldeck, *Microfluid. Nanofluid.*, 2011, **10**, 685–690.
20 Y.-J. Liu, J.-Y. Yang, Y.-M. Nie, C.-H. Lu, E. D. Huang, C.-S. Shin, P. Baldeck and C.-L. Lin, *Microfluid. Nanofluid.*, 2015, **18**, 427–431.
21 J. Lölsberg, J. Linkhorst, A. Cinar, A. Jans, A. J. Kuehne and M. Wessling, *Lab Chip*, 2018, **18**, 1341–1348.
22 A. C. Lamont, A. T. Alsharhan and R. D. Sochol, *Sci. Rep.*, 2019, **9**, 394.
23 J. N. Lee, C. Park and G. M. Whitesides, *Anal. Chem.*, 2003, **75**, 6544–6554.
24 M. Denz, G. Brehm, C. Y. Hémonnot, H. Spears, A. Wittmeier, C. Cassini, O. Saldanha, E. Perego, A. Diaz and M. Burghammer, *et al.*, *Lab Chip*, 2018, **18**, 171–178.
25 R. K. Jena, C. Y. Yue and Y. C. Lam, *Microsyst. Technol.*, 2012, **18**, 159–166.
26 C.-Y. Yen, M.-C. Chang, Z.-F. Shih, Y.-H. Lien and C.-W. Tsao, *Inventions*, 2018, **3**, 49.
27 S. A. Aghvami, A. Opathalage, Z. K. Zhang, M. Ludwig, M. Heymann, M. Norton, N. Wilkins and S. Fraden, *Sens. Actuators, B*, 2017, **247**, 940–949.
28 N. Keller, T. M. Nargang, M. Runck, F. Kotz, A. Striegel, K. Sachsenheimer, D. Klemm, K. Länge, M. Worgull, C. Richter, D. Helmer and B. E. Rapp, *Lab Chip*, 2016, **16**, 1561–1564.
29 P. Ganser, C. Baum, D. Chargin, A. F. Sauer-Budge and A. Sharon, *Biomed. Microdevices*, 2018, **20**, 24.
30 S. Liu, Y. Fan, K. Gao and Y. Zhang, *Mater. Res. Express*, 2018, **5**, 095305.
31 O. Rahmanian and D. L. DeVoe, *Lab Chip*, 2013, **13**, 1102–1108.
32 G. Kumi, C. O. Yanez, K. D. Belfield and J. T. Fourkas, *Lab Chip*, 2010, **10**, 1057.
33 C. N. LaFratta, O. Simoska, I. Pelse, S. Weng and M. Ingram, *Microfluid. Nanofluid.*, 2015, **19**, 419–426.
34 D. Barata, E. Provaggi, C. van Blitterswijk and P. Habibovic, *Lab Chip*, 2017, **17**, 4134–4147.
35 C. Bleilevens, J. Lölsberg, A. Cinar, M. Knoben, O. Grottke, R. Rossaint and M. Wessling, *Sci. Rep.*, 2018, **8**, 8031.
36 J. Greener, W. Li, J. Ren, D. Voicu, V. Pakharenko, T. Tang and E. Kumacheva, *Lab Chip*, 2010, **10**, 522–524.
37 J. Steigert, S. Haeberle, T. Brenner, C. Müller, C. Steinert, P. Koltay, N. Gottschlich, H. Reinecke, J. Rühe and R. Zengerle, *et al.*, *J. Micromech. Microeng.*, 2007, **17**, 333.
38 S. Yadavali, H.-H. Jeong, D. Lee and D. Issadore, *Nat. Commun.*, 2018, **9**, 1222.
39 T. Kohara, *Macromol. Symp.*, 1996, 571–579.
40 E. D. Lemma, F. Rizzi, T. Dattoma, B. Spagnolo, L. Sileo, A. Qualtieri, M. D. Vittorio and F. Pisanello, *IEEE Trans. Nanotechnol.*, 2017, **16**, 23–31.
41 B. Grigoryan, S. J. Paulsen, D. C. Corbett, D. W. Sazer, C. L. Fortin, A. J. Zaita, P. T. Greenfield, N. J. Calafat, J. P. Gounley and A. H. Ta, *et al.*, *Science*, 2019, **364**, 458–464.
42 N. Y. Lin, K. A. Homan, S. S. Robinson, D. B. Kolesky, N. Duarte, A. Moisan and J. A. Lewis, *Proc. Natl. Acad. Sci. U. S. A.*, 2019, **116**, 5399–5404.
43 J. G. Dawson, D. C. Hesley, N. Katagiri, C. P. Nguyen, S. A. Mannuel, T. G. Wun, A. B. Chow, N. R. Gupta, J. V. Bonventre and R. D. Sochol, *2017 IEEE 30th International Conference on Micro Electro Mechanical Systems (MEMS)*, 2017, pp. 426–429.
44 A. C. Lamont, M. A. Restaino, M. J. Kim and R. D. Sochol, *Lab Chip*, 2019, **19**(14), 2340–2345.
45 F. Mayer, S. Richter, J. Westhauser, E. Blasco, C. Barner-Kowollik and M. Wegener, *Sci. Adv.*, 2019, **5**, eaau9160.
46 J. Wang, J. Coburn, C.-P. Liang, N. Woolsey, J. C. Ramella-Roman, Y. Chen and T. J. Pfefer, *Opt. Lett.*, 2014, **39**, 3010–3013.

47 Y. Liu, P. Ghassemi, A. Depkon, M. I. Iacono, J. Lin, G. Mendoza, J. Wang, Q. Tang, Y. Chen and T. J. Pfefer, *Biomed. Opt. Express*, 2018, **9**, 2810–2824.
48 N. Kedia, Z. Liu, R. D. Sochol, J. Tam, D. X. Hammer and A. Agrawal, *Opt. Lett.*, 2019, **44**, 1825–1828.
49 A. Marino, O. Tricinci, M. Battaglini, C. Filippeschi, V. Mattoli, E. Sinibaldi and G. Ciofani, *Small*, 2018, **14**, 1702959.
50 A. C. Scheiwe, S. C. Frank, T. J. Autenrieth, M. Bastmeyer and M. Wegener, *Biomaterials*, 2015, **44**, 186–194.
51 D. Serien and S. Takeuchi, *ACS Biomater. Sci. Eng.*, 2017, **3**, 487–494.
52 B. Richter, V. Hahn, S. Bertels, T. K. Claus, M. Wegener, G. Delaittre, C. Barner-Kowollik and M. Bastmeyer, *Adv. Mater.*, 2017, **29**, 1604342.
53 M. Hippler, E. D. Lemma, S. Bertels, E. Blasco, C. Barner-Kowollik, M. Wegener and M. Bastmeyer, *Adv. Mater.*, 2019, **31**, 1808110.
54 B. Mosadegh, T. Bersano-Begey, J. Y. Park, M. A. Burns and S. Takayama, *Lab Chip*, 2011, **11**, 2813–2818.
55 R. D. Sochol, E. Sweet, C. C. Glick, S. Venkatesh, A. Avetisyan, K. F. Ekman, A. Raulinaitis, A. Tsai, A. Wienkers, K. Korner, K. Hanson, A. Long, B. J. Hightower, G. Slatton, D. C. Burnett, T. L. Massey, K. Iwai, L. P. Lee, K. S. J. Pister and L. Lin, *Lab Chip*, 2016, **16**, 668–678.
56 A. K. Au, N. Bhattacharjee, L. F. Horowitz, T. C. Chang and A. Folch, *Lab Chip*, 2015, **15**, 1934–1941.
57 H. Gong, A. T. Woolley and G. P. Nordin, *Lab Chip*, 2016, **16**, 2450–2458.
58 Y.-S. Lee, N. Bhattacharjee and A. Folch, *Lab Chip*, 2018, **18**, 1207–1214.
59 N. Bhattacharjee, A. Urrios, S. Kang and A. Folch, *Lab Chip*, 2016, **16**, 1720–1742.

